Applied Physics Letters

Role of morphology in defect formation and photo-induced carrier instabilities in amorphous indium oxide

Cite as: Appl. Phys. Lett. **121**, 261902 (2022); https://doi.org/10.1063/5.0128941
Submitted: 01 October 2022 • Accepted: 21 December 2022 • Published Online: 29 December 2022

Julia E. Medvedeva

Applied Physics Letters ARTICLE scitation.org/journal/apl

Role of morphology in defect formation and photo-induced carrier instabilities in amorphous indium oxide

Cite as: Appl. Phys. Lett. **121**, 261902 (2022); doi: 10.1063/5.0128941
Submitted: 1 October 2022 · Accepted: 21 December 2022 ·
Published Online: 29 December 2022

Julia E. Medvedeva[a]

AFFILIATIONS

Physics Department, Missouri University of Science and Technology, Rolla, Missouri 65409, USA

Note: This paper is part of the APL Special Collection on Metal Oxide Thin-Film Electronics.
[a]**Author to whom correspondence should be addressed:** juliaem@mst.edu

ABSTRACT

Ab initio molecular dynamics liquid-quench simulations and hybrid density functional calculations are performed to model the effects of room-temperature atomic fluctuations and photo-illumination on the structural and electronic properties of amorphous sub-stoichiometric $In_2O_{2.96}$. A large configurational ensemble is employed to reliably predict the distribution of localized defects as well as their response to the thermal and light activation. The results reveal that the illumination effects on the carrier concentration are greater in amorphous configurations with shorter In–O bond length and reduced polyhedral sharing as compared to the structures with a more uniform morphology. The obtained correlation between the photo-induced carrier density and the reduction in the number of fully coordinated In-atoms implies that metal oxides with a significant fraction of crystalline/amorphous interfaces would show a more pronounced response to illumination. Photo-excitation also produces In–O_2–In defects that have not been previously found in sub-stoichiometric amorphous oxides; these defects are responsible for carrier instabilities due to overdoping.

Point-defect engineering is a well-developed route to tune the carrier concentration over many orders of magnitude while maintaining high carrier mobility and low optical absorption in crystalline wide-bandgap metal oxides.[1–5] Achieving a similar level of control over the defect formation in amorphous oxide semiconductors is a formidable problem.[6] In marked contrast to crystalline indium oxide where the lattice symmetry limits the structural relaxation to the four nearest neighbors of oxygen vacancy and produces a strongly localized defect state, an oxygen "vacancy" in nearly stoichiometric amorphous indium oxide (a-$In_2O_{2.96}$) is represented by two dozen under-coordinated In atoms—owing to a dramatically increased number of degrees of freedom.[7–10] Consequently, the carrier concentration in amorphous indium oxide (a-IO) is two orders of magnitude higher than that in the crystalline oxide, as observed for the samples grown at the same oxygen pressure.[8] Moreover, when the oxygen stoichiometry is low (a-$In_2O_{2.85}$), the disordered oxide structures feature a percolation-like network of under-coordinated under-shared In–O polyhedra that supports coexistence of shallow, weakly localized, and deep trap states with defect energies ranging from 0.5 to 2.5 eV below the Fermi level.[8,11] Indeed, the observed carrier concentration in a-IO continues to increase steadily with decreasing oxygen pressure, whereas the mobility drops almost six times when the oxygen pressure is reduced from 8 to 1 mTorr.[12] Hence, there are several contradistinctive and often competing mechanisms for carrier generation, carrier scattering, charge compensation, and absorption, making the electron transport and optical transmission hard to control experimentally.

Another crucial factor that sets the crystalline and amorphous ionic oxide phases apart is the degree of structural dynamics and its effects on the defect behavior at elevated temperatures and under illumination. The observed non-equilibrium conductivity in amorphous In-based oxide films exhibits field-effect- and photo-switching transients.[13–18] In binary indium oxide with low crystallization temperature,[12] photo-induced conductivity instabilities are likely to be associated with the crystalline–amorphous transition that is accompanied by a two-order of magnitude change in the carrier density.[7,8,12] In amorphous multi-cation oxides with high crystallization temperature and negligible fraction of nano-crystallinity, the morphology and density of the disordered phase may play a key role in the defect formation and the resulting carrier transport. Indeed, the observed concentration vs mobility relationships differ substantially for the so-called low-quality and high-quality amorphous In–Ga–Zn–O grown by the same deposition technique.[19] The effect of illumination and

room-temperature fluctuations on the structural morphology (i.e., on the coordination distribution and polyhedra sharing, both of which govern defect localization) of a fully amorphous oxide with no crystalline inclusions is not known and is the subject of this work.

In this work, *ab initio* molecular dynamics (MD) simulations and hybrid density functional calculations are performed for amorphous sub-stoichiometric indium oxide to determine how the shallow, weakly localized, and deep traps change upon thermal and/or light activation, affecting the resulting carrier concentration. The amorphous indium oxide structures were obtained using *ab initio* molecular dynamics (MD) liquid-quench simulations as implemented in the Vienna *Ab-initio* Simulation Package (VASP).[20–23] The calculations are based on density functional theory (DFT) with periodic boundary conditions[24,25] and employ Perdew–Burke–Ernzerhof (PBE) exchange–correlation functional[26,27] within the projector augmented-wave method.[28,29] The amorphous structures have been validated by direct comparison of the available experimental Extended X-ray Absorption Fine Structure (EXAFS) spectra and the calculated EXAFS spectra for the MD-simulated structures at different densities.[9] The electronic and optical properties of the PBE-optimized amorphous structures were calculated using hybrid Heyd–Scuseria– Ernzerhof (HSE06) approach[30,31] with a mixing parameter of 0.25 and a screening parameter α of 0.2 $Å^{-1}$ by attaining electronic self-consistency. Specific details of the calculations are given in the supplementary material.

Previously, it was found that amorphous sub-stoichiometric indium oxide structures exhibit bi-modal or multi-modal energy distributions, suggesting that morphology may play an important role in stabilizing the equilibrium configurations.[11] In this work, large statistical ensemble of 80 amorphous configurations is employed in order to predict the probability density of specific modes and also to determine their structural, electronic, and dynamic properties as well as the response to stimuli. Oxygen sub-stoichiometry of $x = 0.074$ in $In_2O_{3-x} = In_{54}O_{79}$, which corresponds to oxygen defect concentration of 11.5×10^{20} cm^{-3}, was chosen because these structures exhibit the formation of both shallow and strongly localized oxygen defects and, hence, represent the widest distribution of defect localization and the energy location of the defect with respect to the Fermi level.[11]

Figure 1 shows the distributions of the calculated enthalpy of formation for DFT-relaxed amorphous $In_2O_{2.926}$ structures with two different densities. First, we find that static-DFT calculations where an

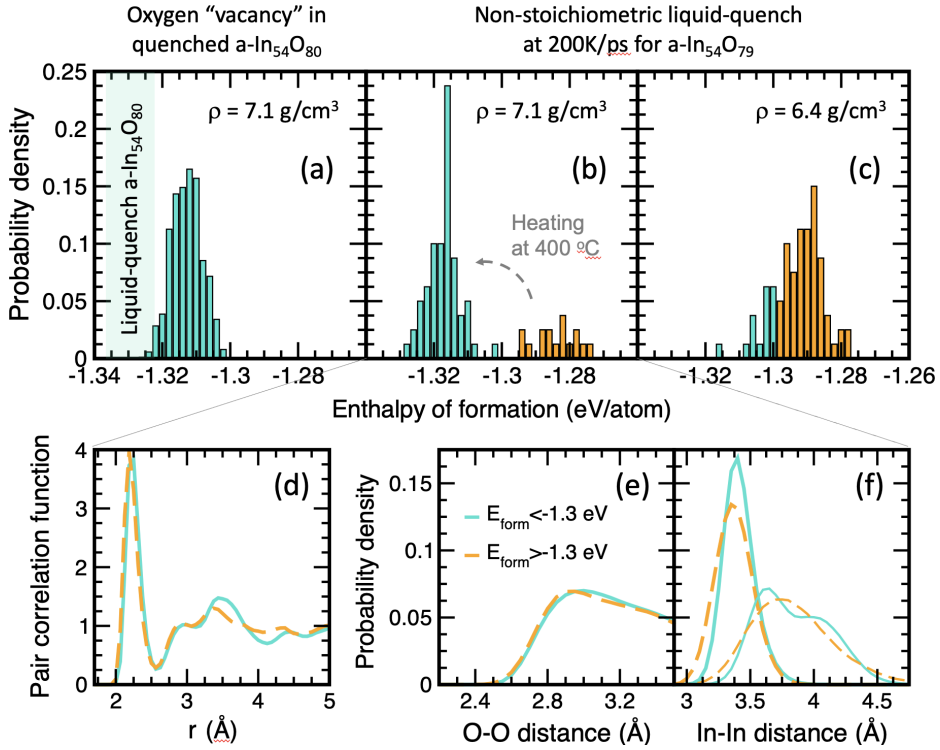

FIG. 1. Distribution of the enthalpy of formation for amorphous $In_{54}O_{79}$ structures obtained by different approaches. (a) The results of 880 static-DFT calculations where a single oxygen "vacancy" is created in 11 quenched amorphous $In_{54}O_{80}$ configurations by taking out each of the oxygen atoms in the supercell and fully relaxing the atomic positions at 0 K. The energy distribution for a-$In_{54}O_{80}$ is shown by the shaded area, whereas the bar plot represents the distribution of 880 calculations for optimized a-$In_{54}O_{79}$. (b) The results of 80 calculations for a-$In_{54}O_{79}$ obtained via non-stoichiometric quench simulations that are performed by setting the oxygen stoichiometry at the melting stage of MD, i.e., prior to cooling. The bi-modal distribution is shown in two colors to mark the difference for the structures with enthalpy of formation above and below –1.3 eV/atom. Heating of the high-energy configurations above 400 °C (via MD simulations with lattice expansion for 5–20 ps) results in lower-energy solutions (see the text). (c) The results of 80 non-stoichiometric quench simulations for a-$In_{54}O_{79}$ with a density of 6.4 g/cm^3, which is 10% below the optimal 7.1 g/cm^3 used in (a) and (b). The same two-color scheme is used for the single-mode distribution to guide the eye. (d) The average pair correlation function calculated for the low-energy (solid line) and high-energy (dashed line) configurations shown in (b). [(e) and (f)] The average O–O and In–In distance distributions calculated for the low-energy (solid line) and high-energy (dashed line) configurations shown in (b). The In–In distribution is further split into edge-shared (think line) and corner-shared (thin line) In–In pairs.

oxygen "vacancy" is created in previously quenched amorphous $In_{54}O_{80}$ structures leads to a single-mode distribution [Fig. 1(a)]. In marked contrast, non-stoichiometric quench simulations for $In_{54}O_{79}$ that are performed by setting the metal-to-oxygen ratio at the melting stage of MD, i.e., prior to cooling, provide lower-energy solutions and, in addition, reveal a bi-modal distribution in the enthalpy of formation values [Fig. 1(b)]. The broad secondary peak accounts for roughly 20% out of the 80 amorphous configurations obtained via the non-stoichiometric MD quench (note that the number of configurations corresponds to 80 oxygen atoms in the randomized supercell at the liquid-phase temperature of 3000 K). The difference between the low- and high-energy structures is only 20–40 meV/atom, and the configurations are stable (showing no energy drift and having similar mean square displacements, see Fig. 1 of the supplementary material) at room temperature and up to 400 °C. Heating the structures at or above 400 °C for 5–20 ps switches several of them to the low-energy configuration upon cooling down and relaxing at zero-K. These findings are in accord with switching of the so-called low-quality amorphous In–Ga–Zn–O samples into high-quality configurations upon heating.[19] Importantly, faster quench rates have little effect on the distribution: at 400 K/ps, there are only two more structures at high-energy out of 80 cases as compared to 200 K/ps. Additional non-stoichiometric quench simulations for $In_{54}O_{79}$ with lower density, Fig. 1(c), result in a shift of the distribution toward higher energies and a single-mode behavior, suggesting that differences in the short- and/or medium-range morphology might be the reason for the bi-modal energy distribution for the DFT-optimal density of 7.1 g/cm^3. A comparison of the pair correlation functions calculated as an average for the configurations with the enthalpy of formation below and above −1.3 eV, Fig. 1(d), reveals a slight shift in the first-shell peak and major differences for the interatomic distances greater than 3.5 Å. Indeed, negligible differences are found in the O–O distance distributions, whereas both edge- and corner-shared In–In distance distributions feature shorter In–In distances and suppressed or shifted peaks in the high-energy amorphous structures [Figs. 1(e) and 1(f)].

Several structural characteristics are found to distinctly represent the low- and high-energy configurations obtained from the non-stoichiometric MD quench simulations [Figs. 2(a)–2(c)]. Specifically, the high-energy structures have smaller In–O (first-shell) effective coordination, shorter In–O bond length, and smaller number of shared In neighbors as compared to the corresponding values for the low-energy cases [Figs. 2(a)–2(c)]. The distributions for other structural parameters overlap for the low- and high-energy cases (Fig. 2 of the supplementary material). Thus, despite the identical stoichiometry, density, and MD simulation parameters (i.e., the initial melting temperature and cooling rate), two distinct morphologies with different

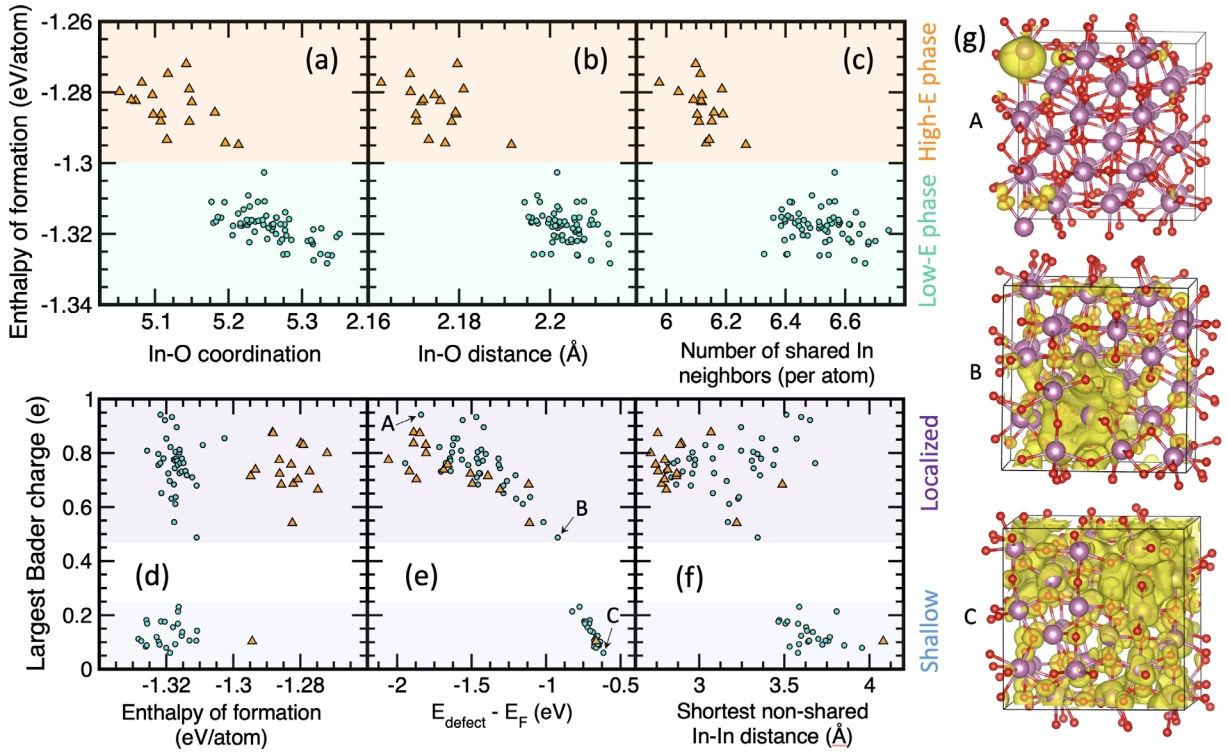

FIG. 2. The structural and electronic properties of 80 a-$In_{54}O_{79}$ configurations with different energy and degree of electron localization. [(a)-(c)] The average In–O effective coordination, the average In-O effective distance, and the average number of shared In neighbors in each of the amorphous structures shown as a function of the corresponding enthalpy of formation. (d) The calculated largest Bader charge in each amorphous configuration for low-energy (circle) and high-energy (triangle) cases. (e) The energy location of the defect state with respect to the Fermi level in each configuration shown for shallow and localized states as determined by the largest Bader charge. (f) The shortest In–In distance for non-shared pairs as a function of the largest Bader charge for each a-$In_{54}O_{79}$. (g) The charge density distribution in the supercell for the representative electronic states—a strongly localized deep trap state (A), a weakly localized state (B), and a shallow state (C). The three cases are marked in (e).

short and medium-range characteristics have been obtained for amorphous $In_2O_{2.926}$. The structures with lower enthalpy of formation feature longer In–O distances, hence, higher In–O coordination, larger fraction of fully coordinated In atoms, and larger number of polyhedra sharing, and smaller polyhedral distortions—as compared to the values of the high-energy cases. Larger number of shared polyhedra represents a more efficient polyhedra packing in the disordered structure, in accord with the lower enthalpy of formation.

The distinct structural morphology in the low- and high-energy configurations may entail differences in the electronic properties. Figures 2(d)–2(f) plot the largest Bader charge calculated in each of the 80 amorphous configurations as well as its dependence on the defect energy with respect to the Fermi level and on the shortest non-shared In–In distance in the given structure. We find that all but one high-energy configurations contain strongly localized defects that trap an electron and are located 1–2 eV below the Fermi level. Most of these deep defects can be identified by the short non-shared In–In distance that signifies the formation of a metallic bond, in agreement with earlier reports.[8,11] Conversely, about 36% of the low-energy configurations correspond to a shallow (delocalized) electronic state; the remaining structures contain localized or strongly localized trap states, similar to those found in the high-energy cases. Importantly, the energies for the low-energy configurations with localized and delocalized defects are indistinguishable, Fig. 2(d), suggesting that the states are likely to coexist, whereas the transformations from a deep bound to a shallow state or vice versa may occur at no energy cost, as indeed shown in this work [see Figs. 3(a) and 3(e) of the supplementary material]. The charge density distribution in the supercell for the representative electronic states is shown in Fig. 2(g).

Now, each of the 80 amorphous structures with various electronic states was subjected to (i) thermal activation at room temperature; (ii) light activation at 0 K, i.e., without thermal motion of atoms; and (iii) short and prolonged light activation at room-temperature that allows thermally induced structural reconfiguration of the charged state. All charged states were modeled by the removal of four valence electrons from the system that corresponds to both O defects in a-$In_{54}O_{79}$ being doubly charged (see Fig. 4 of the supplementary material).

Figure 3(a) shows the carrier concentration after the specific thermal or light treatment. The number of carriers calculated as an integrated density of states within ± 0.1 eV from the Fermi level is given as an average value for the low-energy structures that contain shallow

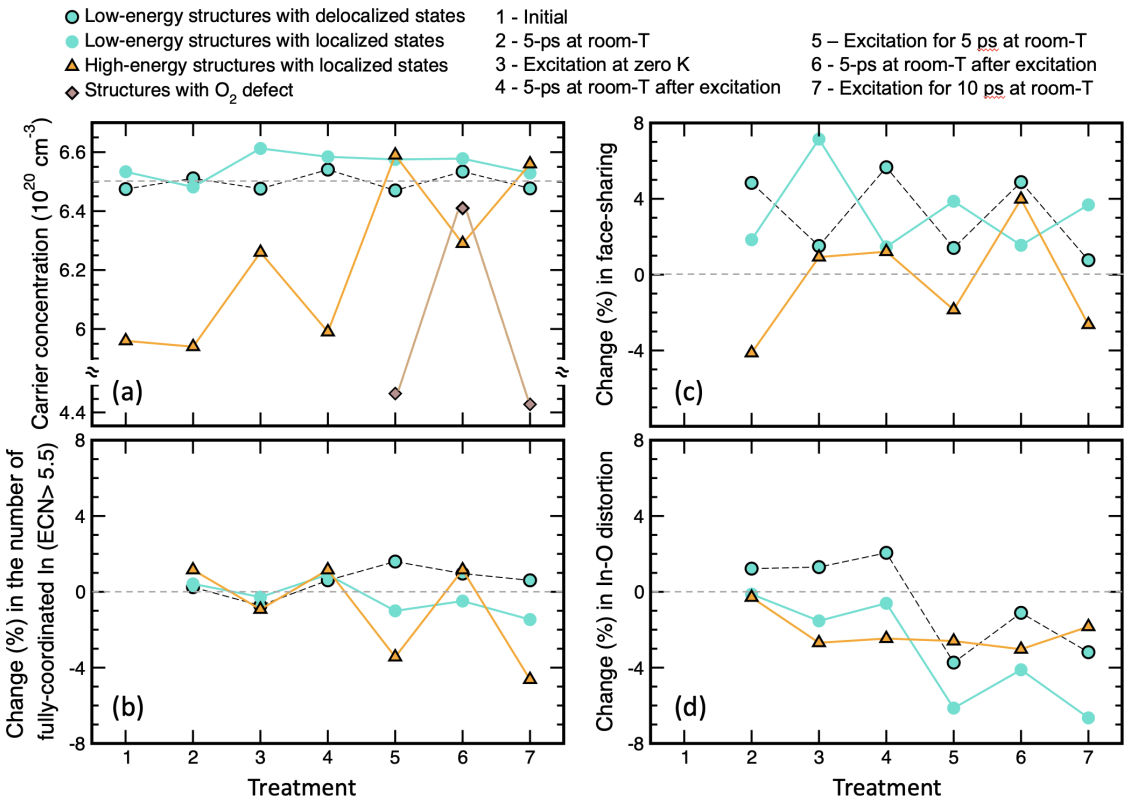

FIG. 3. The calculated carrier concentration and select structural parameters for a-$In_{54}O_{79}$ after thermal and/or light treatments marked as 2–7 in the x-axis (see legends and text for more details). The results for 80 structures are presented as an average over the following groups: the low-energy shallow state cases (circle, solid line), the low-energy localized state cases (circle, dashed line); the high-energy localized state cases (triangle); and the low- and high-energy structures with O_2 defect formed (diamond). (a) The number of carriers is given as an average value for the structures in the specified group. (b–d) The calculated average percent change with respect to the value in the initial amorphous structure after each treatment. The changes in eight other structural characteristics investigated in this work are at or well below 1% (see the supplementary material).

(delocalized) states; the low-energy structures contain localized and deep trap states [those with the largest Bader charge values of 0.4 or above, cf. Fig. 2(d)] and the high-energy structures. We find that, with one exception discussed below, the carrier concentration in the delocalized states is nearly insensitive to the thermal or light treatment: room-temperature thermal motion slightly increases the number of carriers, whereas excitation (with or without thermal motion of the atoms) returns the carrier density back to the initial value. In these configurations, the lack of two oxygen atoms in the supercell is represented by the largest fraction of under-coordinated In atoms, so that the charge density distribution within the conduction band is uniform. In these cases, an electron excitation within the partially filled conduction band does not increase carrier density—the excited electrons simply return back to the initial delocalized state.

For the low-energy structures with a localized defect, the largest increase in the carrier concentration is found after excitation at zero-K, i.e., when no thermal motion of atoms is allowed and only zero-K DFT-relaxation is performed for the charged state and also after returning to the neutral state [Fig. 3(a)]. An electron excitation from the localized or deep trap states into the conduction band is expected to increase the carrier concentration. However, the results suggest that thermal motion—especially, for the prolonged light activation—diminish the gains. Further analysis suggests that thermal fluctuations facilitate an extended bond reconfiguration well beyond the next-nearest neighbors of the defect that may help create another deep defect upon returning to the neutral state.

Finally, photo-excitation in the high-energy structures results in significantly larger increase in the carrier concentration as compared to the low-energy cases [Fig. 3(a)]. At the same time, thermal reconfiguration after zero-K excitation reduces the carrier concentration to the initial value (which means that the excited electron returns to the initial or a newly formed localized state). It also reduces the carrier gains to nearly one half after the room-temperature excitation. Therefore, only upon a continuous illumination at room temperature, the carrier concentration may reach and maintain the values similar to those in the low-energy structures.

For the majority of low- and high-energy cases, illumination (with the subsequent return to the neutral state) leads to a slight decrease in the enthalpy of formation, Figs. 3(a)–3(d) of the supplementary material, likely, due to an improved morphology upon the structural rearrangement caused by the electron excitation. At the same time, we find that about 13% of the low-energy structures and about 18% of the high-energy structures have a significantly higher energy after the light activation that is accompanied by the room-temperature structural reconfiguration. Further analysis reveals that these configurations possess an In–O_2–In defect with the O–O distance of about 1.5 Å and both oxygen atoms bonded to In atoms, also known as peroxylinkages[32] or peroxide bridge[33] in a silica glass. While the peroxide defect is common in the perfectly stoichiometric amorphous indium oxide,[8,9] none of the 80 initial sub-stoichiometric structures or the 80 structures after room-temperature activation, or after heating to 400 °C and subsequent cooling back, or after zero-K excitation and subsequent room-temperature relaxation, has an O_2 defect formed. This highlights the role of atomic reconfiguration during the photo-illumination as the reason for the peroxide formation in sub-stoichiometric amorphous indium oxide. The structural analysis reveals that the O_2 defects are always formed within a cluster of fully or over-coordinated In atoms, this is in accord with previous results for the O_2 formation near the crystalline–amorphous In_2O_3 interface.[34] The photo-induced formation of the O_2^{2-} defect in sub-stoichiometric amorphous indium oxide releases two free electrons and leads to conduction band overdoping and a pronounced drop in the carrier concentration [Fig. 3(a)]. Room temperature fluctuations in the dark nearly instantly break all O_2 defects, so that the carrier concentration recovers. (Note, in stoichiometric indium oxide without light exposure, the O_2 defect was shown to be stable up to 1100 K.[8]) At the same time, prolonged light exposure of a-$In_{54}O_{79}$ helps maintain the majority of the peroxide defects: after 10 ps room-temperature excitation, two new structures with a peroxide appear and in one configuration the O_2 breaks (in this case, the average coordination of the neighboring In atoms is the lowest among all cases with peroxide), while the overall number of the light-exposed structures with the O_2 defect and, hence, a reduced carrier density, appears to saturate at about 15% of the total configurations.

To explain the carrier concentration behavior under various treatments, we compare 11 parameters that describe the short-range (nearest-neighbor) and medium-range (polyhedral sharing) structures for each treated configuration to the corresponding values in the initial a-$In_{54}O_{79}$. The largest structural deviations are shown in Figs. 3(b)–3(d), whereas the remaining eight parameters vary by less than 1%, see the supplementary material, on average over the number of configurations within the specified group. Most importantly, we find that the changes in the number of fully coordinated In atoms (CN > 5.5) inversely correlate with the changes in the carrier density in the high-energy structures. This means that the photo-excitation of an electron from localized state requires the fully coordinated In atoms give away their O neighbor(s) to compensate the lack of oxygen at the charged defect. The light-induced changes correspond to coordination redistribution, whereas the overall In coordination varies at most by 0.5% (see Fig. 5 of the supplementary material). In addition, we find that illumination affects the number of face-shared In–In pairs;[11] these structural defects may play a role in the structural dynamics upon light activation. Last but not least, light-exposure reduces the polyhedral distortions in all configurations that point to an improved carrier mobility.

In summary, the results of systematic computational modeling for thermal and light activation in amorphous sub-stoichiometric indium oxide reveal that the largest changes in the number of carriers occur due to the photo-induced formation of O_2 defects that overdopes the system. Compared to the low-energy structures with a more uniform morphology, the higher-energy configurations with reduced polyhedra sharing (that resembles a low-density morphology) show larger reduction in the number of fully coordinated In atoms that correlates with the gains in the carrier density upon photo-illumination. The light-induced coordination transformations suggest that a similar behavior should be expected at the crystalline/amorphous interfaces of the structures with nano-crystalline inclusions or in multi-phase indium oxide or in crystallized samples with a large fraction of grain boundaries. In such structures, conductivity instabilities upon illumination will be much more pronounced—owing to the two-order magnitude difference in the carrier concentration between the crystalline and amorphous indium oxides.

See the supplementary material for the additional data on the structural and electronic properties of 80 configurations before and after temperature and light treatment.

The author acknowledges the support from the National Science Foundation (NSF) DMREF program (Grant Nos. DMR-1729779 and DMR-1842467) and from the Department of Energy (DOE), Office of Energy Efficiency and Renewable Energy (EERE), SETO FY20 program (Grant No. DE-EE0009346). The computational resources were provided by Missouri S&T and by NSF-MRI program (Grant No. OAC-1919789).

AUTHOR DECLARATIONS

Conflict of Interest

The authors have no conflicts to disclose.

Author Contributions

Julia Medvedeva: Conceptualization (equal); Data curation (equal); Formal analysis (equal); Funding acquisition (equal); Investigation (equal); Methodology (equal); Project administration (equal); Resources (equal); Software (equal); Supervision (equal); Validation (equal); Visualization (equal); Writing – original draft (equal); Writing – review & editing (equal).

DATA AVAILABILITY

The data that support the findings of this study are available from the corresponding author upon reasonable request.

REFERENCES

[1]C. Kilic and A. Zunger, "Origins of coexistence of conductivity and transparency in SnO_2," Phys. Rev. Lett. **88**, 95501 (2002).
[2]C. G. V. de Walle, "Strategies for controlling the conductivity of wide-band-gap semiconductors," Phys. Stat. Solidi B **229**, 221–228 (2002).
[3]S. Lany and A. Zunger, "Dopability, intrinsic conductivity and nonstoichiometry of transparent conducting oxides," Phys. Rev. Lett. **98**, 045501 (2007).
[4]A. Murat, A. U. Adler, T. O. Mason, and J. E. Medvedeva, "Carrier generation in multicomponent wide-bandgap oxides: $InGaZnO_4$," J. Am. Chem. Soc. **135**, 5685–5692 (2013).
[5]F. Gunkel, D. V. Christensen, Y. Z. Chen, and N. Pryds, "Oxygen vacancies: The (in)visible friend of oxide electronics," Appl. Phys. Lett. **116**, 120505 (2020).
[6]K. Ide, K. Nomura, H. Hosono, and T. Kamiya, "Electronic defects in amorphous oxide semiconductors: A review," Phys. Status Solidi A **216**, 1800372 (2019).
[7]J. E. Medvedeva, D. B. Buchholz, and R. P. Chang, "Recent advances in understanding the structure and properties of amorphous oxide semiconductors," Adv. Electron. Mater. **3**, 1700082 (2017).
[8]J. Medvedeva, I. Zhuravlev, C. Burris, D. Buchholz, M. Grayson, and R. Chang, "Origin of high carrier concentration in amorphous wide-bandgap oxides: Role of disorder in defect formation and electron localization in In_2O_{3-x}," J. Appl. Phys. **127**, 175701 (2020).
[9]J. Medvedeva, in *Amorphous Oxide Semiconductors: IGZO and Related Materials for Display and Memory*, Edited by H. Hosono and H. Kumomi (Wiley, 2022).
[10]J. E. Medvedeva and B. Bhattarai, "Hydrogen doping in wide-bandgap amorphous In–Ga–O semiconductors," J. Mater. Chem. C **8**, 15436–15449 (2020).
[11]J. E. Medvedeva, E. Caputa-Hatley, and I. Zhuravlev, "Metallic networks and hydrogen compensation in highly nonstoichiometric amorphous In_2O_{3-x}," Phys. Rev. Mater. **6**, 025601 (2022).
[12]D. B. Buchholz, Q. Ma, D. Alducin, A. Ponce, M. Jose-Yacaman, R. Khanal, J. E. Medvedeva, and R. P. Chang, "The structure and properties of amorphous indium oxide," Chem. Mater. **26**, 5401–5411 (2014).
[13]T.-C. Fung, C.-S. Chuang, K. Nomura, H-P. D. Shieh, H. Hosono, and J. Kanicki, "Photofield-effect in amorphous In-Ga-Zn-O (a-IGZO) thin-film transistors," J. Inf. Disp. **9**, 21–29 (2008).
[14]P. Migliorato, M. Delwar Hossain Chowdhury, J. Gwang Um, M. Seok, and J. Jang, "Light/negative bias stress instabilities in indium gallium zinc oxide thin film transistors explained by creation of a double donor," Appl. Phys. Lett. **101**, 123502 (2012).
[15]J. K. Jeong, "Photo-bias instability of metal oxide thin film transistors for advanced active matrix displays," J. Mater. Res. **28**, 2071–2084 (2013).
[16]C.-H. Han, S.-S. Kim, K.-R. Kim, D.-H. Baek, S.-S. Kim, and B-. D. Choi, "Effects of electron trapping and interface state generation on bias stress induced in indium-gallium-zinc oxide thin-film transistors," Jpn. J. Appl. Phys. **53**, 08NG04 (2014).
[17]A. J. Flewitt and M. J. Powell, "A thermalization energy analysis of the threshold voltage shift in amorphous indium gallium zinc oxide thin film transistors under simultaneous negative gate bias and illumination," J. Appl. Phys. **115**, 134501 (2014).
[18]J. Luo, "Characterizing and modeling transient photo-conductivity in amorphous In-Ga-Zn-O thin films," Ph.D. thesis (Northwestern University, 2016).
[19]T. Kamiya, K. Nomura, and H. Hosono, "Origins of high mobility and low operation voltage of amorphous oxide TFTs: Electronic structure, electron transport, defects and doping," J. Disp. Technol. **5**, 273–288 (2009).
[20]G. Kresse and J. Hafner, "Ab initio molecular dynamics for liquid metals," Phys. Rev. B **47**, 558–561 (1993).
[21]G. Kresse and J. Hafner, "Ab initio molecular-dynamics simulation of the liquid-metal–amorphous-semiconductor transition in germanium," Phys. Rev. B **49**, 14251–14269 (1994).
[22]G. Kresse and J. Furthmuller, "Efficient iterative schemes for ab initio total-energy calculations using a plane-wave basis set," Phys. Rev. B **54**, 11169–11186 (1996).
[23]G. Kresse and J. Furthmuller, "Efficiency of ab-initio total energy calculations for metals and semiconductors using a plane-wave basis set," Comput. Mater. Sci. **6**, 15–50 (1996).
[24]P. Hohenberg and W. Kohn, "Inhomogeneous electron gas," Phys. Rev. **136**, B864–B871 (1964).
[25]W. Kohn and L. J. Sham, "Self-consistent equations including exchange and correlation effects," Phys. Rev. **140**, A1133–A1138 (1965).
[26]J. P. Perdew, K. Burke, and M. Ernzerhof, "Generalized gradient approximation made simple," Phys. Rev. Lett. **77**, 3865–3868 (1996).
[27]J. P. Perdew, K. Burke, and M. Ernzerhof, "Generalized gradient approximation made simple [Phys. Rev. Lett. 77, 3865 (1996)]," Phys. Rev. Lett. **78**, 1396–1396 (1997).
[28]P. E. Blochl, "Projector augmented-wave method," Phys. Rev. B **50**, 17953–17979 (1994).
[29]G. Kresse and D. Joubert, "From ultrasoft pseudopotentials to the projector augmented-wave method," Phys. Rev. B **59**, 1758–1775 (1999).
[30]J. Heyd, G. E. Scuseria, and M. Ernzerhof, "Hybrid functionals based on a screened Coulomb potential," J. Chem. Phys. **118**, 8207–8215 (2003).
[31]J. Heyd, J. E. Peralta, G. E. Scuseria, and R. L. Martin, "Energy band gaps and lattice parameters evaluated with the Heyd-Scuseria-Ernzerhof screened hybrid functional," J. Chem. Phys. **123**, 174101 (2005).
[32]H. Hosono, H. Kawazoe, and N. Matsunami, "Experimental evidence for Frenkel defect formation in amorphous SiO_2 by electronic excitation," Phys. Rev. Lett. **80**, 317–320 (1998).
[33]A. Shluger and E. Stefanovich, "Models of the self-trapped exciton and nearest-neighbor defect pair in SiO_2," Phys. Rev. B **42**, 9664 (1990).
[34]J. E. Medvedeva, K. Sharma, B. Bhattarai, and M. I. Bertoni, "Hydrogen behavior at crystalline/amorphous interface of transparent oxide semiconductor and its effects on carrier transport and crystallization," ACS Appl. Mater. Interfaces **14**, 39535–39547 (2022).